Available online at www.sciencedirect.com
ScienceDirect
Trans. Nonferrous Met. Soc. China 35(2025) 1137−1154
Transactions of Nonferrous Metals Society of China
www.tnmsc.cn

Effect of Ca addition on microstructure and properties of porous Mg−1Zn−1Sn alloy scaffold prepared via 3D printed Ti template-infiltration casting

Lei-ting YU[1], Hao LIU[1], Peng-nan JIANG[1], Shao-yuan LYU[1,2], Yun ZHAO[1,2], Wei LI[1,2,3], Min-fang CHEN[1,2,3]

1. School of Materials Science and Engineering, Tianjin University of Technology, Tianjin 300384, China;
2. National Demonstration Center for Experimental Function Materials Education,
Tianjin University of Technology, Tianjin 300384, China;
3. Key Laboratory of Display Materials and Photoelectric Device (Ministry of Education),
Tianjin University of Technology, Tianjin 300384, China

Received 24 August 2023; accepted 9 April 2024

Abstract: The Mg−1Zn−1Sn and Mg−1Zn−1Sn−0.2Ca alloy scaffolds were prepared via infiltration casting using 3D-printed Ti templates to achieve complete and accurate control of the pore structure. The results indicate that the actual porosity and pore size of the prepared P model for each pore size are greater than the designed values. The addition of Ca changes the second phase of the alloy from Mg_2Sn to CaMgSn and refines its microstructure. The compressive yield strength and compressive modulus of the Mg−1Zn−1Sn−0.2Ca alloy scaffold reach 32.61 MPa and 0.23 GPa, respectively. The corrosion current density is measured at 14.64 $\mu A/cm^2$, with an instantaneous corrosion rate of 0.335 mm/a. Both scaffolds exhibit excellent biocompatibility and no cytotoxicity. Additionally, the antibacterial effects of both alloys on *E. coli* are greater than 97.81%. These results indicate that Mg alloy scaffolds have great potential for clinical applications.

Key words: infiltration casting; 3D-printed Ti template; mechanical properties; corrosion resistance; biocompatibility

---

1 Introduction

Bone defects caused by tumors, orthopedic inflammation, and external trauma require bone grafting. Degradable metal materials have become a research hotspot for bone defect repair materials because of their good mechanical properties, unique corrosion and degradation characteristics, and ability to be metabolized by the human body. These materials include Mg-, Zn-, and Fe-based materials [1−3]. However, each type of degradable metal has limitations. The degradation rate of Fe-based materials is too slow, and their degradation products are not easily absorbed by the surrounding tissues, requiring a second operation. Zn-based materials exhibit certain cytotoxicities [4], and their development is limited by work softening and self-aging [5−7]. Mg and its alloys have an elastic modulus close to that of the natural cortical bone [8]; thus, porous Mg alloy scaffolds can be utilized to replace cancellous bone. Porous Mg alloy scaffolds have adjustable mechanical strengths, and Mg^{2+} released from Mg alloy degradation in the body fluid environment can enhance blood vessel formation in new bone tissues and guide bone and blood vessel growth [9]. Various methods have been developed for preparing porous Mg alloy scaffolds,

---

Corresponding author: Min-fang CHEN, Tel: +86-22-60216916, E-mail: mfchentj@126.com;
Wei LI, Tel: +86-22-60216916, E-mail: weilitjut@126.com

DOI: https://doi.org/10.1016/S1003-6326(24)66739-7

including investment casting, melt foaming, powder metallurgy, traditional infiltration casting, and metal additive manufacturing (3D printing). Powder metallurgy and traditional infiltration casting can be used to prepare porous Mg alloy scaffolds with completely interconnected pore structures. However, these two methods cannot accurately control the internal pore structures of the Mg alloy scaffolds.

In contrast, 3D printing technology allows the creation of scaffolds with internal pore structures and complex shapes, such as triply periodic minimal surface (TPMS) models, which have smooth surfaces and highly connected pores. The overall structure was precisely controlled by an implicit function, which is an excellent solution for the design and modeling of porous structures. The P model has good connectivity and controllability of the 3D surface structure and has an advantage over conventional porous structures in terms of structural efficiency. However, Mg has a high chemical activity, which makes Mg alloy powder preparation difficult, and the powder composition is not easy to blend. Additionally, the inherent characteristics of Mg alloys, such as their low evaporation temperature, high vapor pressure, and high oxidation tendency, lead to powder splashing and hot cracking during 3D printing. Therefore, the preparation of Mg alloy scaffolds by 3D printing still faces a series of challenges, and slight carelessness may increase the risk of explosion [10].

The preparation of porous Mg alloy scaffolds by infiltration casting pure Ti templates using 3D printing can address the problems of powder preparation and printing defects in the 3D printing of Mg alloys. Pure Ti is a completely non-toxic metal with a high melting point, and the process of powder preparation and 3D printing is well-developed; therefore, the structure of the printed template can be much closer to the design model. Additionally, the infiltration casting process is also well-developed and can be used to prepare dense alloys, which can effectively prevent the formation of defects such as molten balls, porosity, and thermal cracks. Alloying is one of the most effective ways to improve the corrosion resistance and mechanical properties of Mg alloys [11]. Both Zn and Sn are essential elements in the human body and have good biocompatibility. The addition of appropriate amounts of Zn and Sn can effectively enhance the mechanical properties and corrosion resistance of Mg alloy [12,13], promote tissue growth, and improve the activity of various enzymes [14]. Ca is primarily stored in the bones and teeth and can promote bone healing. Ca alloying can refine the microstructure and reduce the grain size of Mg alloys, improving their properties [15]. YANG et al [16] studied the effects of Ca addition on the microstructure and mechanical properties of cast Mg−5Zn−5Sn (wt.%) alloy. The results showed that adding 1.5−5.5 wt.% Ca to the Mg−5Zn−5Sn alloy not only refined the microstructure of the Mg alloy but also promoted the formation of a thermally stable CaMgSn phase, which enhanced the tensile mechanical properties and creep properties of the Mg alloy. WEI et al [17] investigated the effects of Ca addition (0, 0.2, 0.4, and 0.6 wt.%) on the microstructure and mechanical properties of Mg−4.5Zn−4.5Sn−2Al alloy. The results showed that the grain size and grain boundary compounds of the alloy gradually decreased with increasing Ca content; however, the mechanical properties decreased progressively, possibly because of the susceptibility of the Mg alloy with more than 0.3 wt.% Ca to thermal cracking [18]. KIM et al [19] confirmed through electrochemical and immersion experiments that the addition of Ca improved the corrosion resistance of Mg−Al−Sn alloy. The alloying elements can not only improve the properties of Mg alloys but can also be absorbed or discharged by the human body after degradation [20]. Therefore, Zn, Sn, and Ca have been widely used as alloying elements in the construction of medical Mg alloy implants.

This study aims to prepare biodegradable porous Mg alloy scaffolds with internal fully connected pores and precisely controllable pore structures using a novel approach and to regulate the mechanical properties and corrosion resistance of porous Mg alloy scaffolds by alloying and pore size control of the model. The clinical conversion potential of the Mg alloy scaffolds was evaluated based on their microstructure, mechanical properties, corrosion resistance, biocompatibility, and antibacterial properties.

2 Experimental

2.1 Model design of porous scaffold pore structure

A combination of computer-aided design and mathematical modeling of the TPMS method was used to design the pore structures of Mg alloy scaffolds. Three primitive (P) models with pore sizes of 1000 μm (large pore: LP), 800 μm (medium pore: MP), and 500 μm (small pore: SP), with porosities of 50%, were designed, as shown in Fig. 1. The 3D models were imported into a BLT-S200 series 3D metal printer (Huaxing Advanced Science and Technology Application Research (Tianjin) Co., Ltd., China), and a pure Ti template was prepared. The particle size of pure Ti spherical powder (Chendu Huayin Powder Technology Co., Ltd., China) used was 15−53 μm. The laser scanning speed was 1500 mm/s, and the laser power was 500 W. Unidirectional powder laying was adopted, and the single-layer powder thickness was 0.02 mm. High-purity Ar was injected into the printing process to eliminate the negative effects of evaporation and other harmful gases. Finally, porous pure Ti templates with dimensions of 16 mm × 16 mm × 16 mm were obtained. After printing, the printed pure Ti templates were stripped from the Ti substrate using the wire-cutting method and ultrasonically cleaned with anhydrous alcohol to remove the excess powder in the pores.

2.2 Mg alloy scaffold prepared by infiltration casting

The preparation process of the porous Mg alloy scaffold using a 3D-printed Ti template as the pore structure is illustrated in Fig. 2. Pure Mg ingots (99.99 wt.%), pure Zn particles (99.99 wt.%), pure Sn particles (99.99 wt.%), and Mg−Ca intermediate alloys (25 wt.% Ca) were used as raw materials. The Mg−1Zn−1Sn (ZT11) and Mg−1Zn−1Sn−0.2Ca (ZTX110) alloys were melted at 760 °C under the protection of a gas mixture containing 99.6% N_2 and 0.4% SF_6. After allowing the melt to stand for 15 min, the Mg alloy melt was quickly poured into a steel mold preheated at 690 °C and placed in pure Ti templates. N_2 gas was quickly injected into the mold until the melt completely penetrated the pure Ti templates. After rapid water cooling, the mold was released to obtain an

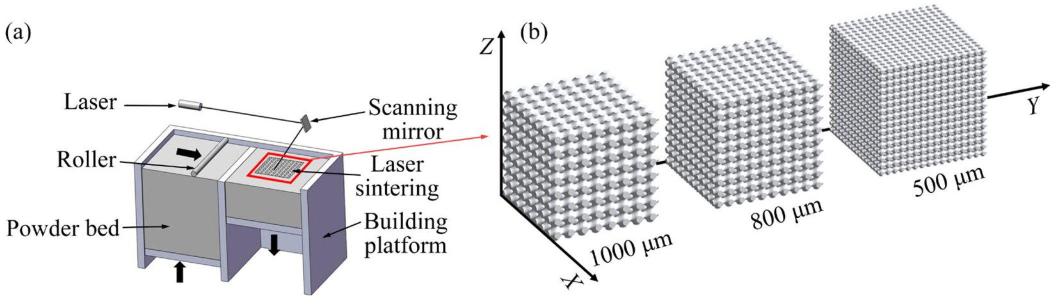

Fig. 1 Accurately 3D-printed pure Ti templates: (a) Preparation of porous pure Ti by selective laser melting; (b) Designed P models with different pore sizes

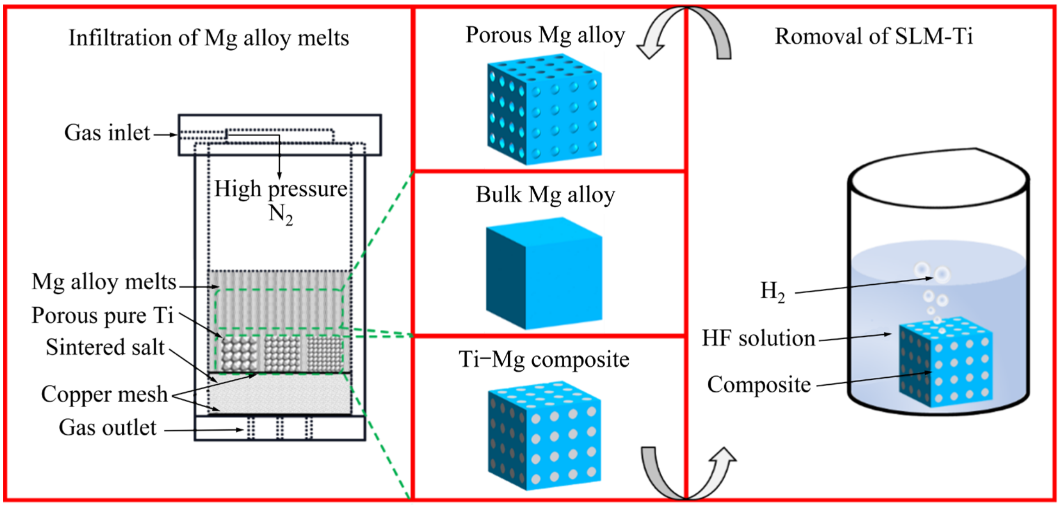

Fig. 2 Preparation flow chart of infiltration casting porous Mg alloy scaffold with 3D-printed Ti template

intermediate complex ingot of pure Ti and Mg alloys. The ingot was wire-cut into *d*6 mm × 9 mm and 6 mm × 6 mm × 3 mm intermediate complex samples, which were washed and dried. The porous Mg alloy scaffold was obtained by the elution of a pure Ti template with 40 wt.% HF solution. In addition, the upper bulk Mg alloy ingot was wire-cut into 6 mm × 6 mm × 3 mm samples for phase analysis to determine the corrosion resistance of the Mg alloy in vitro and the porosity of the porous Mg alloy scaffolds.

2.3 Pore structure characterization

The pore structures of the scaffolds were observed under a microscope, and the actual pore sizes of the LP, MP, and SP samples were measured using Nano Measurer 1.2. The mass method [21] was used to determine the actual porosity of the LP, MP, and SP samples. The actual porosity (P_a) was calculated using Eq. (1):

$$P_a=1-V_1/V_2=1-\rho V_1/\rho V_2=1-M_1/M_2 \quad (1)$$

where V_1 is the scaffold volume, V_2 is the bulk volume with the same shape (6 mm × 6 mm × 3 mm) as the scaffold, ρ is the density of Mg alloy, M_1 is the mass of the scaffold, and M_2 is the mass of the bulk Mg alloy with the same shape (6 mm × 6 mm × 3 mm) as the scaffold. At least three samples were analyzed for each group.

2.4 Phase analysis and microstructure characterization

Phase analysis of bulk ZT11 and ZTX110 alloys was performed by X-ray diffraction (XRD, Ultima IV, Japan) using Cu K_α rays (λ=0.15418 nm) at 40 kV and 100 mA. The scanning rate was 3 (°)/min, and the scanning range was 20°−80°. The surface of the bulk sample was mechanically ground with 320# to 3000# SiC sandpaper. It was then mechanically polished and chemically etched. The etching solution consisted of 3.75 g of picric acid, 5 mL of acetic acid, 5 mL of deionized water, and 45 mL of anhydrous ethanol. The microstructure and grain size were observed by optical microscopy (OM; GX51F, Japan) and scanning electron microscopy (SEM; Quanta FEG 250, USA). The mean particle size of the Mg alloy was measured using Nano Measurer 1.2. The composition of the second phase was quantitatively analyzed using energy-dispersive spectroscopy (EDS; Quanta FEG 250, USA).

2.5 Mechanical properties test

The porous compressed specimens were machined according to ISO 13314—2011, and the size of the compressed specimens was *d*6 mm × 9 mm. The compression test was performed using a universal testing machine (DDL50, China) at a compression speed of 0.5 mm/min at room temperature. Three parallel specimens were used in each group. The compressive yield strength was calculated using the 0.2% offset method [22].

2.6 Corrosion resistance test

(1) Electrochemical tests

The electrochemical polarization (IE) and impedance spectroscopy (EIS) were performed in Hank's solution using a three-electrode system with an electrochemical workstation (Zennium, Zahner, Germany). Prior to the EIS and IE experiments, the surfaces of all samples were ground with 3000# SiC sandpaper, and the samples were tested for open-circuit potential (OCP) to stabilize them. The EIS experiments were first performed in the frequency range from 100 mHz to 10 kHz, and the IE experiments were then performed at a scan rate of 1 mV/s. Each group consisted of three parallel samples to ensure accuracy and stability. The instantaneous corrosion rate (P_i, mm/a) was calculated using Eq. (2), where J_{corr} is the corrosion current density:

$$P_i=22.85J_{corr} \quad (2)$$

(2) Hydrogen evolution test

A porous sample was immersed in Hank's solution. As the degradation of 1 mol Mg (24.31 g) releases 1 mol H_2 (22.4 L), it can be inferred that each release of 1 mL H_2 is equivalent to the degradation of 1.085 mg Mg. Therefore, the average annual degradation rate of the sample was calculated based on the volume of H_2 released over a period of time while the sample was immersed in Hank's solution. The annual corrosion rates (C_r, mm/a) of the samples were calculated using Eq. (3):

$$C_r=K\Delta m/(\rho\cdot A\cdot t) \quad (3)$$

where K is a constant (8.76×10^4), ρ is the density of the sample (1.74 g/cm^3), Δm is the mass loss of the volume conversion of H_2 collected (g), A is the initial surface area of the sample (cm^2), and t is the immersed time (h).

(3) In vitro quasi-in-situ corrosion test

A diamond cutter (SYJ−150, China) was used to draw cross-lines on the surface of each sample to observe the microstructure at the same position before and after immersion. The samples were immersed in Hank's solution, washed with anhydrous ethanol, and then dried. The corroded surfaces of the samples were observed using OM at different immersion time.

2.7 Second phase potential test

The PeakFroce KPFM-AM mode of an atomic force microscope (AFM; Dimension icon, Bruker) was used to measure the second phase potential of the ZT11 and ZTX110 alloys. The sample size for the AFM testing was 6 mm × 6 mm × 3 mm. A silicon probe coated with a Pt−Cr layer was used, and the data were post-processed using NanoScope Analysis.

2.8 Cytocompatibility test

(1) Indirect method (MTT test)

According to the national standard GB/T 16886.12, *α*-MEM (containing 10% FBS, Gibco, 100 U/mL Pen, and 100 μg Str. Genview) was used as an extraction transmitter to prepare the extraction solution. The UV-sterilized scaffold samples were placed in a 37 °C cell incubator for 24 h at constant temperature based on the ratio of surface area to extraction transmitter of 1.25 cm^2/mL, sterile filtration was performed through an injection filter (aperture ≤0.22 μm) to obtain the extract (100%). The extract was diluted to obtain concentrations of 50%, 25%, and 12.5%. MC-3T3 cells were cultured with above *α*-MEM, then digested with 0.25% Trypsin-EDTA (Genview, China), counted under a microscope (Nikon, Ti-SR, Japan), and the cell suspension concentration was adjusted to 1.0×10^5 cells/mL. A cell suspension (100 μL) was added into each well of the 96-well plate and cultured for 24 h to ensure adhesion. After determining the growth state, the medium in the experimental group was replaced with the extracts at different concentrations. After incubation for 1, 2, and 3 d, 10 μL of Thiazolyl Blue (MTT, $C_{18}H_{16}BrN_5S$, Genview, China) was added to each well. After continuous culture for 4 h, the medium was removed and the plate was washed twice with phosphate buffered saline (PBS). DMSO (150 μL, C_2H_6OS, Dingguo, China) was added for 10 min and then the plate was tested. The absorbance (OD) of each well was measured using an enzyme-labeled instrument (PL−9602, Perlong, China). The wavelength of the light was 492 nm. Cell viability (C_v) was determined from absorbance readings and calculated using Eq. (4):

$$C_v=(O_e-O_c)/(O_b-O_c)\times100\% \tag{4}$$

where O_e is the absorbance of the experimental group, O_c is the absorbance of the control group, and O_b is the absorbance of the blank group. The evaluation criterion was as follows: if the cell survival rate was >50%, the sample was regarded as non-cytotoxic [23]. The MTT assay was repeated three times with five samples each time.

(2) Direct method (cell co-culture)

MC-3T3 cells (1.0×10^5 cells/mL) were seeded on the surface of the scaffold, cultured for 24 h, washed three times with PBS, and treated for 30 min in 4% paraformaldehyde (PFA, AR-0211, China). The fixed cells were dehydrated with gradient ethanol at concentrations of 50%, 70%, 90%, and 100% and then treated with gold spray after air drying. The cell morphology and adhesion were observed using SEM.

2.9 Antibacterial experiment

The antibacterial activities of the ZT11 and ZTX110 alloys were evaluated using gram-negative *Escherichia coli* (*E. coli*). 10 μL of the bacterial solution was placed in a test tube, and 1 mL of deionized water was added. The bulk sample was placed in a test tube and co-cultured with the bacterial solution on a shaking table at 37 °C for 24 h. Then, the co-cultured bacterial solution was diluted 1 million times with deionized water, and 100 μL of the diluted mixed solution was dropped on the AGAR plate for spin coating. Finally, the AGAR plate was cultured in an incubator at 37 °C and taken out for photos after 24 h. The antibacterial rate (A_r) was calculated using Eq. (5):

$$A_r=\frac{N_b-N_e}{N_b} \tag{5}$$

where N_b is the number of colonies in the blank group, and N_e is the number of colonies in the experimental group.

3 Results

3.1 Pore structure

Figure 3 shows the pure Ti pore structure

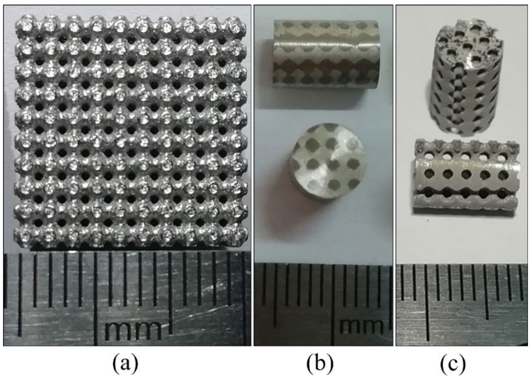
(a) (b) (c)

Fig. 3 Prepared pure Ti templates, Ti−Mg composites, and porous Mg scaffolds: (a) Pure Ti pore structure template prepared by 3D printing; (b) Intermediate complex of pure Ti and Mg alloy; (c) Porous Mg alloy scaffolds after elution with HF solution

template prepared by 3D printing, the intermediate complex of pure Ti and Mg alloy, and the porous Mg alloy scaffold after elution with HF solution. The 3D-printed pure Ti template has a metallic luster and is well formed. The interface of the pure Ti and Mg alloy intermediate complex is tight, and there are no casting defects. The Mg alloy scaffold exhibits a complete pore structure. To further verify the degree of interfacial bonding between the pure Ti and the Mg alloy intermediate complex, the interface was observed by SEM, and the results are shown in Fig. 4. The SEM images and mapping EDS diagram show that there are no gaps at the interface of the pure Ti and the Mg alloy, indicating excellent bonding in the pure Ti/Mg intermediate complex created through infiltration casting. The pure Ti template is removed from the pure Ti/Mg alloy intermediate complex based on the different reactions of Ti and Mg in the HF solution. A series of chemical reactions occur when the pure Ti/Mg alloy intermediate complex sample is eluted using a pure Ti template at a 40 wt.% HF solution, in which Ti can be gradually corroded by chemical reaction (6):

$$Ti+6HF \rightarrow H_2TiF_6+2H_2\uparrow \quad (6)$$

When Ti is dissolved in HF solution, it can be converted to TiF_6^{2-} in the soluble ionized state. This process continues until all Ti is completely consumed. The release of H_2 is only a sign of Ti dissolution. Simultaneously, Mg reacts with the HF solution via reaction (7) to form a relatively dense MgF_2 coating on the scaffold surface. This MgF_2 coating is sufficiently dense to hinder further reactions between HF and Mg:

$$Mg+2HF \rightarrow MgF_2+H_2\uparrow \quad (7)$$

Figure 5 shows the actual measured porosities and pore sizes of the Mg alloy scaffolds with different pore sizes (LP, MP, and SP). The actual porosities of the P models with LP, MP, and SP are 58.6%, 60.3%, and 63.6%, respectively, and the actual pore sizes are 1043.65, 844.14, and 609.02 μm, respectively. As the design pore sizes of the Mg alloy scaffolds decrease, the actual porosities increase gradually, and the increment of actual pore sizes also increases. This is caused by the corresponding increase in the surface area as the pore sizes decrease. The largest increment is observed in the SP model, with a difference of 109.02 μm. During 3D printing, the powder in the heat-affected zone adheres to the molten pool owing to heat transfer. The larger the surface area, the greater the adhesion of the powder. Therefore, during the solidification of the molten pool, the pure Ti template with SP has the most adhered powder, which increases the error in the 3D-printed

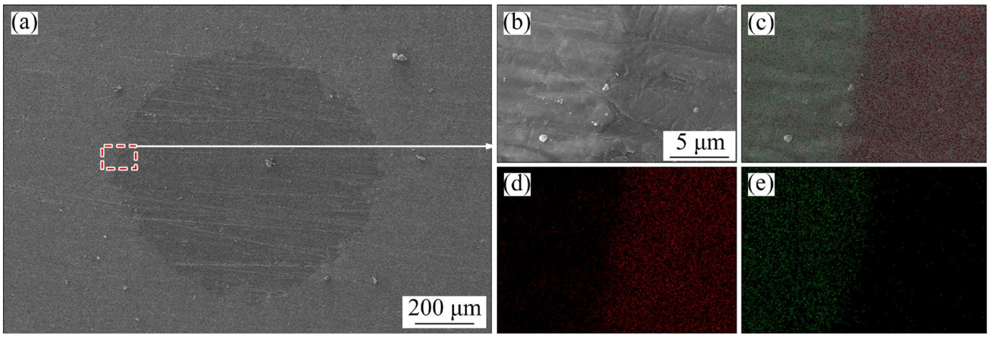

Fig. 4 Interface bonding of Ti and Mg alloy intermediate complex prepared by infiltration casting: (a) Pure Ti and Mg alloy intermediate complex interface; (b) Enlarged view of box in (a); (c) Mixed distribution of Mg and Ti elements; (d) Distribution of Mg elements; (e) Distribution of Ti elements

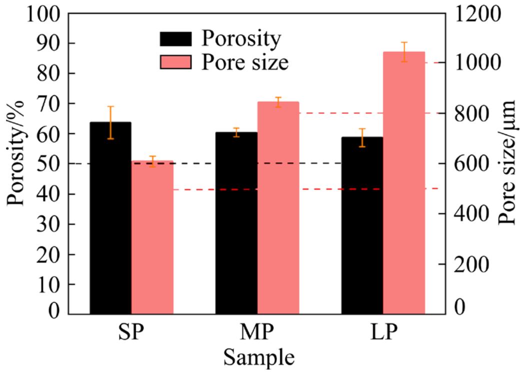

Fig. 5 Measured actual porosities and actual pore sizes of P model Mg alloy scaffolds with different pore sizes (LP, MP and SP) (The dotted lines are the design porosity and pore size)

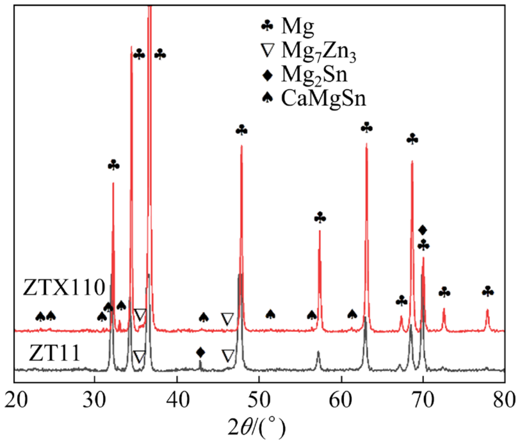

Fig. 6 XRD patterns of ZT11 and ZTX110 alloys

pure Ti template. In other words, the actual volume of the pure Ti template increases, leading to an increase in both the pore sizes and porosities of the Mg alloy scaffolds, which are higher than the designed values.

3.2 Phase composition

The phase analysis results for the ZT11 and ZTX110 alloys are shown in Figs. 6 and 7. Among them, Fig. 6 shows the XRD patterns of the bulk ZT11 and ZTX110 alloys. As shown in Fig. 6, the ZT11 alloy contains Mg, Mg_7Zn_3, and Mg_2Sn phases, whereas the ZTX110 alloy contains Mg, Mg_7Zn_3, and CaMgSn phases. The second phase of the alloy changes from Mg_2Sn to CaMgSn after adding Ca. Figures 7(a−d) show the OM and SEM microstructures of the bulk ZT11 and ZTX110 alloys. After adding Ca to ZT11 alloy, the number of second phases is significantly increased, and the second phase is smaller and more dispersed in the structure. At the same time, the grain of the ZTX110 alloy is refined from 203.93 to 108.40 μm (Figs. 7(e−f)). To further determine the category of the second phase, a point scan was performed at the positions in Figs. 7(c, d). Table 1 lists the proportions of each element at Points A−F. Points A and D are the matrix components of the ZT11 and ZTX110 alloys, respectively. It is shown that 0.53 at.% Zn and 0.48 at.% Sn are in the ZT11 alloy matrix, and 0.68 at.% Zn and 0.14 at.% Sn are in the ZTX110 alloy. Combined with the XRD results (Fig. 6), it is determined that Point B is the Mg_7Zn_3 phase and Mg_2Sn phase, and Point C is the Mg_7Zn_3 phase. The Sn/Ca molar ratios of Points E and F are approximately 1; therefore, they are both CaMgSn phases. As the bulk Mg alloys and porous Mg alloy scaffolds were prepared by infiltration casting from

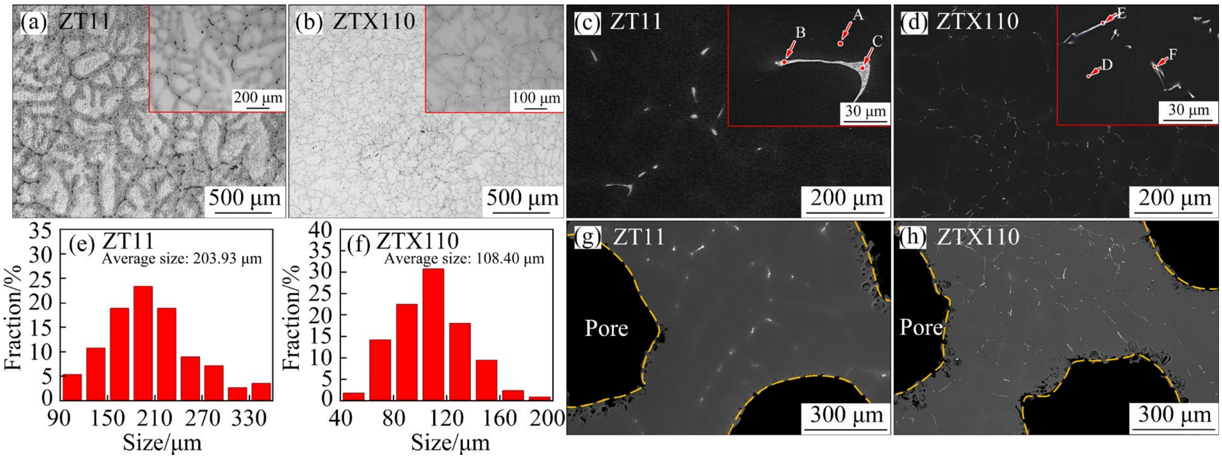

Fig. 7 Microstructures of ZT11 and ZTX110 alloys: (a, b) OM microstructures of bulk ZT11 and ZTX110 alloys; (c, d) SEM microstructures of bulk ZT11 and ZTX110 alloys; (e, f) Average grain sizes of ZT11 and ZTX110 alloys; (g, h) SEM microstructures of ZT11 and ZTX110 alloy scaffolds

Table 1 EDS analysis results of Points A−F for ZT11 and ZTX110 alloys in Figs. 7(c, d)

Element	Point A		Point B		Point C		Point D		Point E		Point F	
	wt.%	at.%	wt.%	at.%	wt.%	at.%	wt.%	at.%	wt.%	at.%	wt.%	at.%
Mg	96.31	98.99	63.96	85.44	65.48	83.75	97.53	99.18	51.82	77.80	43.18	71.13
Zn	1.39	0.53	21.04	10.46	33.73	16.04	1.80	0.68	0.49	0.27	0.57	0.35
Sn	2.30	0.48	15.00	4.10	0.79	0.21	0.67	0.14	35.62	10.95	41.83	14.11
Ca	−	−	−	−	−	−	0.00	0.00	12.06	10.98	14.42	14.41

the same batch, they are considered to have the same type and distribution as the second phase. Figures 7(g, h) confirm that the scaffold prisms exhibit a microstructure similar to that of the bulk alloy. Furthermore, it is evident that the addition of Ca refines the structure and second phase of the ZTX110 alloy.

3.3 Mechanical properties of Mg alloy scaffolds

Figure 8 shows the compressive mechanical properties of ZT11 and ZTX110 alloys with different pore sizes (LP, MP, and SP). The compression process can be divided into four stages: elastic, yield, stress plateau, and dense. Table 2 lists the compressive yield strength and compressive modulus of the ZT11 and ZTX110 alloys with different pore sizes (LP, MP, and SP). As can be seen from Fig. 8 and Table 2, the compressive yield strength and compressive modulus of the ZT11 and ZTX110 alloys both increase with increasing pore sizes. This is because, with an increase in the pore sizes, the diameter of the pillar around the pore increases, and the resistance to external forces increases. In addition, the compressive yield strength and compressive modulus of the ZTX110 alloy are higher than those of the ZT11 alloy for two alloys with the same pore sizes. This is because the second phase type of the alloy changes after the addition of Ca, thus playing the role in second phase strengthening. Finally, the compressive yield strength and compressive modulus of the LP-ZTX110 scaffold are the highest, which are 32.61 MPa and 0.23 GPa, respectively. In addition, the fluctuation of the stress–strain curve in Fig. 8 implies that the scaffold is gradually broken, indicating that the scaffold can withstand large deformations. Even if 50% compression strain is applied, an overall brittle fracture does not occur [24].

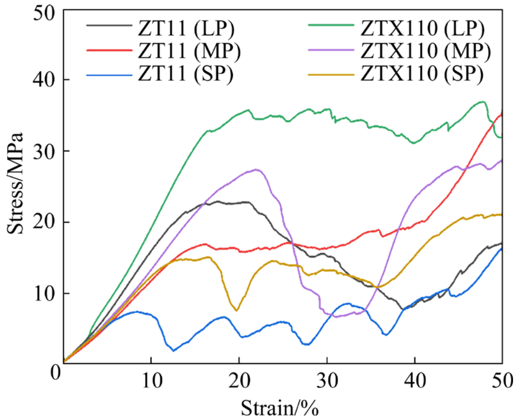

Fig. 8 Compressive stress–strain curves of ZT11 and ZTX110 alloys with different pore sizes (LP, MP, and SP)

Table 2 Compressive yield strength (YCS) and compressive modulus of ZT11 and ZTX110 alloys with different pore sizes (LP, MP, and SP)

Sample	YCS/MPa	Compressive modulus/GPa
ZT11 (LP)	20.95±1.94	0.18±0.02
ZT11 (MP)	15.76±1.22	0.13±0.01
ZT11 (SP)	6.45±1.93	0.11±0.03
ZTX110 (LP)	32.61±1.32	0.23±0.01
ZTX110 (MP)	23.98±0.61	0.16±0.01
ZTX110 (SP)	13.79±3.54	0.13±0.03

Figure 9 shows the macroscopic states of the ZT11 and ZTX110 alloy scaffolds at different time points during compression with different pores (LP, MP, and SP). As shown in Fig. 9, different pore sizes exhibit similar phenomena at the same time point. When the sample is compressed for 120 s, the pore shape changes and the sample width increases. When compressed for 240 s, the vertical pillars of the sample begin to bend and deform, the pores collapse, the pores begin to close, and the width of the sample continues to increase. Simultaneously, the pillars of the sample begin to undergo shear fracture along the horizontal direction. As the deformation continues to increase, the pores in the sample close until compaction. During the entire compression process, a large range of stress

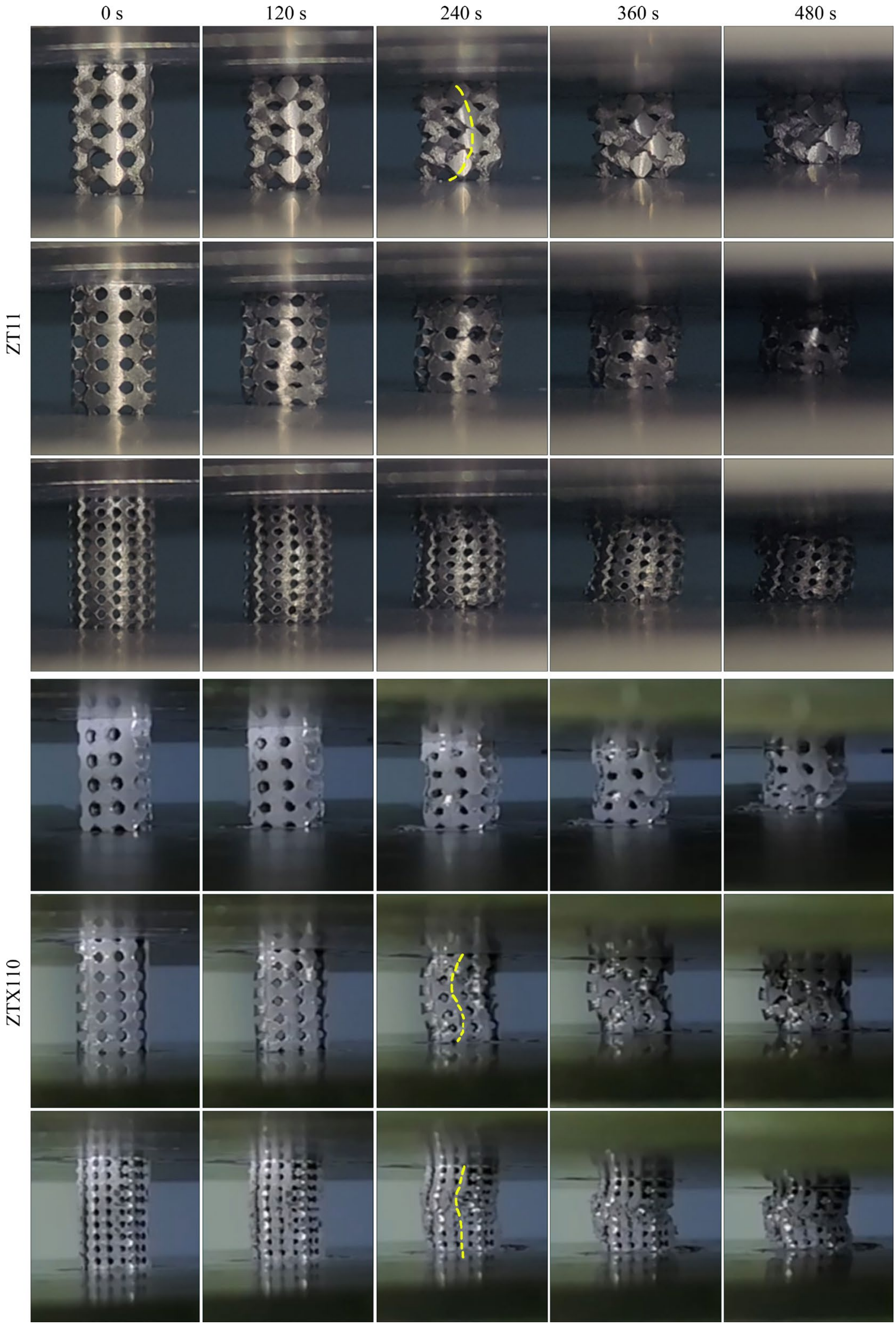

Fig. 9 Macroscopic states of ZT11 and ZTX110 alloy scaffolds with different pores (LP, MP, and SP) during compression at different time points

fluctuations appear in the stress platform stage of the compressive stress–strain curves of some samples, which may have been caused by the deviation of the pores in the horizontal direction (yellow dashed line in Fig. 9). It is practically impossible to ensure that the two surfaces of the scaffold and the loading head are also perfectly parallel to the surface [25].

3.4 Corrosion resistance

Because porous scaffolds are prone to short-circuiting the working electrodes during electrochemical testing, bulk alloys were used for electrochemical testing. Figure 10 shows the OCP, IE curves, EIS spectrum, and fitting circuit diagrams of the bulk ZT11 and ZTX110 alloys. OCP is the potential of the sample system when the current is zero. At OCP, the sample is in a state of self-corrosion. There is an incubation period before the OCP reaches a steady state. Generally, the longer the incubation period, the better the corrosion resistance. As shown in Fig. 10(a), the OCP of the ZTX110 alloy in Hank's solution first stabilizes, indicating that its corrosion is uniform and slow. Table 3 lists the electrochemical data of the ZT11 and ZTX110 alloys in Hank's solution, as shown in Fig. 10(b). From Table 3 and Fig. 10(b), it can be observed that the ZTX110 alloy has a lower J_{corr}. The cathode IE curve shows the hydrogen evolution reaction on the alloy surface [26,27]. The IE curve shows that the ZTX110 alloy has a low current density at the same potential; therefore, the hydrogen evolution reaction on the surface of the ZTX110 alloy is relatively mild. The anode IE curve shows the dissolution rate of the material [26,28]. The anode IE curves of the ZTX110 and ZT11 alloys nearly overlap, indicating that the anode dissolution rates of the ZTX110 and ZT11 alloys do not differ significantly. The J_{corr} is obtained using the Tafel extrapolation method. J_{corr} represents the electron transfer rate during the electrochemical process and reflects the corrosion rate. ZTX110 alloy has a lower J_{corr} (14.64 μA/cm^2), which indicates that ZTX110 alloy has better corrosion resistance. The P_{i} calculated using Eq. (2) shows that the P_{i} value of the ZTX110 alloy is small (0.335 mm/a), indicating that its corrosion resistance is good. As shown in Fig. 10(b), both alloys contain two capacitive rings in the high- and low-frequency regions. The large diameter of the capacitive ring of ZTX110 alloy indicates that the charge transfer is strongly inhibited, alloy degradation is slow, and the corrosion product film formed is stable. This is consistent with the behavior of J_{corr}. Figure 10(d) shows the electrochemical impedance equivalent circuit fitted using ZSimpWin. The solution resistance (R_{s}), electric double-layer capacitance ($\mathrm{CPE_{dl}}$), charge-transfer resistance (R_{ct}), $Mg(OH)_2$ film resistance (R_{f}), and

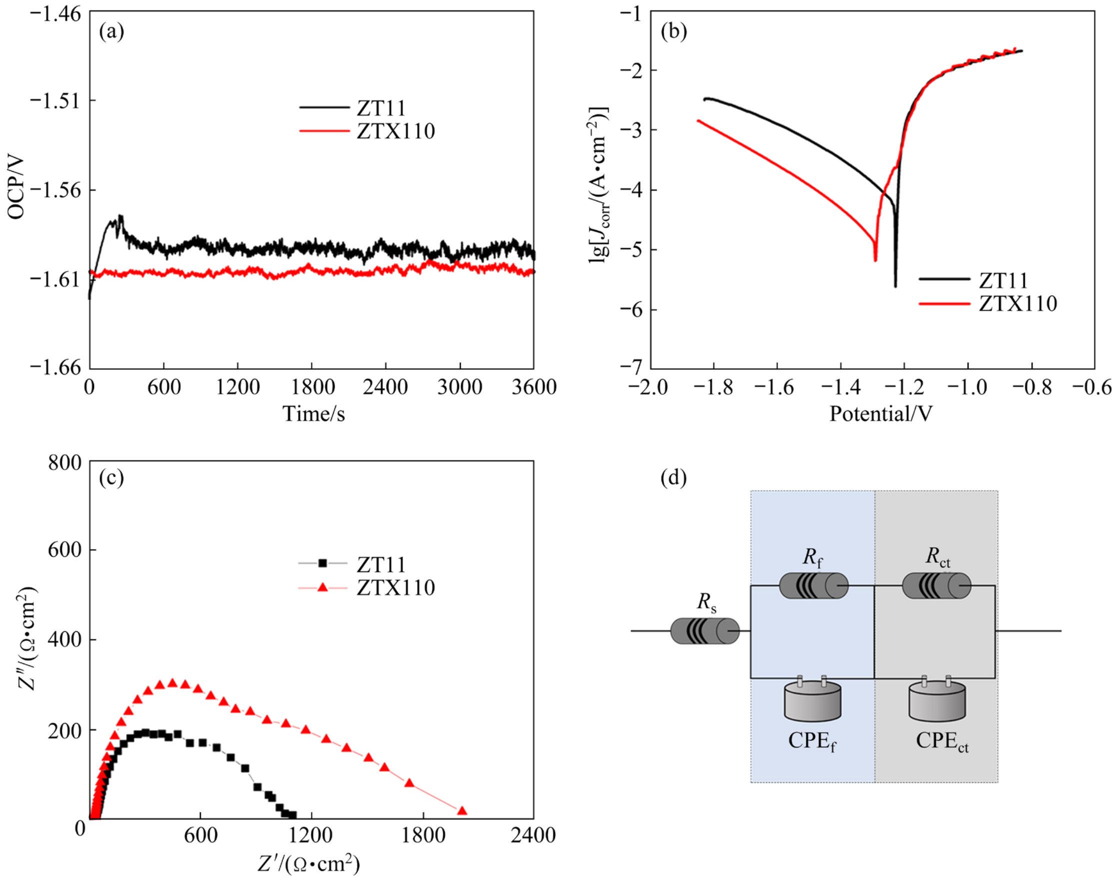

Fig. 10 OCP (a), IE curve (b), EIS spectrum (c), and fitted circuit diagram (d) of bulk ZT11 and ZTX110 alloys

Table 3 Electrochemical data of ZT11 and ZTX110 alloys in Hank's solution

Sample	φ_{corr}/V	J_{corr}/(μA·cm^{-2})	P_i/(mm·a^{-1})
ZT11	−1.229	58.74	1.342
ZTX110	−1.295	14.64	0.335

$Mg(OH)_2$ film capacitance (CPE_f) constitute the equivalent circuit that reflects the entire electrode. Table 4 lists the electrochemical parameters of both alloys obtained by fitting the EIS data. It can be seen that the polarization resistance R_p ($R_p=R_{ct}+R_f$) [29] of the ZTX110 alloy is larger, indicating that it has lower activity and better corrosion resistance in Hank's solution. The calculated EIS results agreed well with those of the IE curve.

Figure 11 shows the C_r of hydrogen evolution in the ZT11 and ZTX110 alloy scaffolds with different pore sizes (LP, MP, and SP). From Fig. 11, it can be seen that the corrosion resistance of the ZT11 alloy scaffolds increases as the pore sizes increase, and the SP-ZT11 alloy scaffold fails after 16 h following hydrogen evolution, the MP-ZT11 alloy scaffold fails after 28 h following hydrogen evolution, and the LP-ZT11 alloy scaffold fails after 36 h following hydrogen evolution. The C_r values at failure are 37.43, 21.17, and 11.38 mm/a, respectively. The corrosion resistance of the ZTX110 alloy scaffolds also increases with increasing pore sizes, and the SP-ZTX110 alloy, MP-ZTX110 alloy, and LP-ZTX110 scaffolds fail after 48, 103, and 199 h, respectively. The C_r values at failure are 7.76, 2.00, and 0.88 mm/a, respectively. The results show that the corrosion resistance of the ZTX110 alloy scaffold is significantly higher than that of the ZT11 alloy scaffold.

3.5 Cell biocompatibility

Figure 12 shows the cell survival rates of the ZT11 and ZTX110 alloy scaffolds at different extraction concentrations for 1, 2, and 3 d. As shown in Fig. 12, the cell survival rates of the ZT11 alloy scaffolds at 1, 2, and 3 d are generally higher than those of the ZTX110 alloy scaffolds. This is because the C_r content of the ZT11 alloy scaffolds is higher than that of the ZTX110 alloy scaffolds, and more Mg^{2+} is released in the extract, thus promoting the growth of cells. Notably, the cell survival rates of the ZT11 and ZTX110 alloy scaffolds are higher than 75% at 1, 2, and 3 d under different extraction concentrations. Therefore, it can be concluded that the ZT11 and ZTX110 alloy scaffolds have excellent biocompatibility and no cytotoxicity. Figure 13 shows the morphologies of cell adhesion on the sample surface during the direct cell co-culture of the ZT11 and ZTX110 alloy scaffolds. As shown in Fig. 13, the ZT11 alloy scaffold has more corrosion products than the ZTX110 alloy scaffold. From the enlarged image, it

Table 4 Values of electrochemical parameters obtained by fitting EIS

Sample	R_s/(Ω·cm^2)	R_{ct}/(Ω·cm^2)	CPE_{dl}/(Ω^{-1}·s^n·cm^{-2})	n_{dl}	R_f/(Ω·cm^2)	CPE_f/(Ω^{-1}·s^n·cm^{-2})	n_f
ZT11	32.36	190	4.80×10^{-5}	1	781.2	3.87×10^{-4}	0.58
ZTX110	28.06	428.6	1.17×10^{-5}	0.99	1070	4.37×10^{-4}	0.5

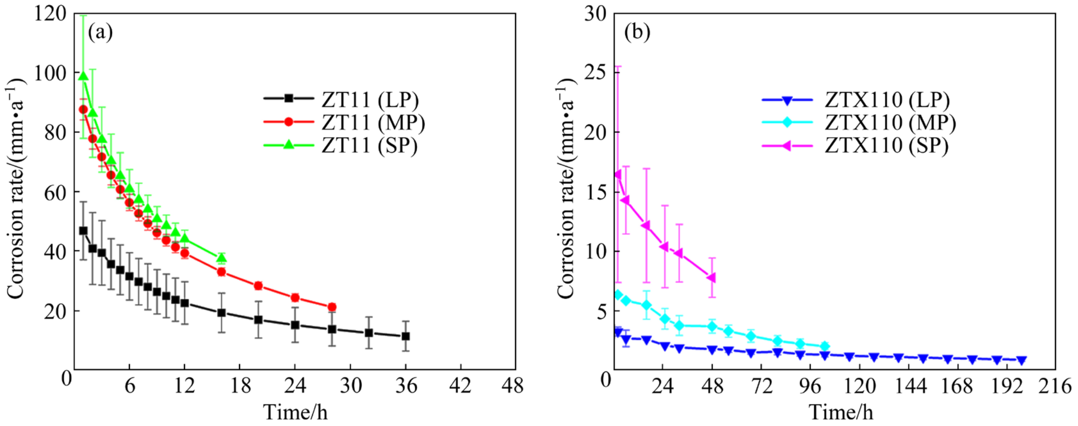

Fig. 11 C_r of hydrogen evolution for scaffolds with different pore sizes: (a) ZT11 alloy scaffold; (b) ZTX110 alloy scaffold

can be observed that on the surface of the ZT11 alloy scaffold, MC-3T3 cells adhere to the gaps between the corrosion product particles and filamentous pseudopods entangled on the corrosion product particles. On the surface of the ZTX110 alloy scaffold, only a small amount of corrosion products are observed; hence, the MC-3T3 cells have enough space to spread on the surface of the scaffold. Therefore, compared to the ZT11 alloy scaffold, the MC-3T3 cells have a larger adhesion area on the surface of the ZTX110 alloy scaffold.

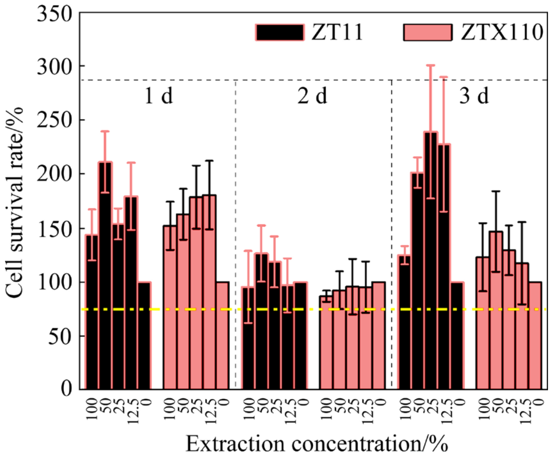

Fig. 12 Cell survival rates of ZT11 and ZTX110 alloy scaffolds at different extraction concentrations for 1, 2, and 3 d

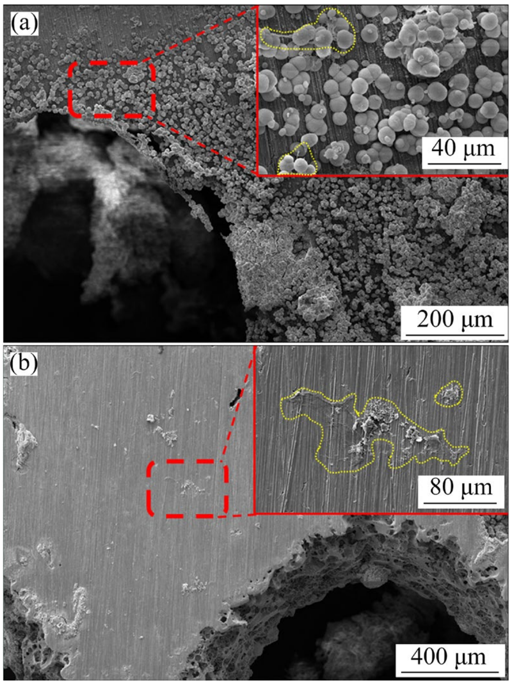

Fig. 13 Adhesion morphologies of MC-3T3 cells on different alloy scaffolds: (a) ZT11 alloy scaffolds; (b) ZTX110 alloy scaffolds

3.6 Antibacterial property

Because of the presence of the MgF_2 coating on the surface of the scaffolds, bulk alloys were used to test their antibacterial properties. Figure 14 shows the results of the antibacterial sensitivity testing of the bulk ZT11 and ZTX110 alloys to *E. coli* in the AGAR plate medium evaluated by the planking method. An AGAR plate culture medium without material was used as a blank group. Results show that the ZT11 and ZTX110 alloys have a good antibacterial effect on *E. coli*, with an antibacterial rate higher than 97.81%. Furthermore, the antibacterial activity of ZT11 against *E. coli* is higher than that of ZTX110. This is primarily caused by the lower corrosion resistance of the ZT11 alloy, resulting in a higher release of Sn^{2+}/Sn^{4+} during the degradation process, thereby improving the antibacterial properties of the Mg alloy. An increase in pH value can lead to the alkalization of the microenvironment, which can also effectively resist bacterial growth [30]. However, it has been shown that the antibacterial effect caused by alkalization is weaker than that of antibacterial metal ions [31].

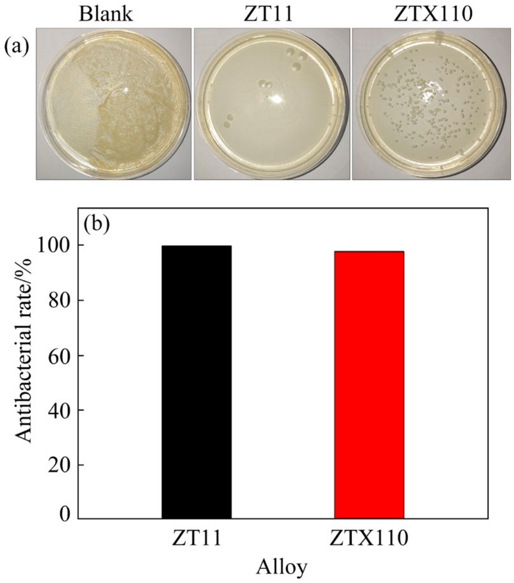

Fig. 14 Antibacterial sensitivity test results: (a) Antibacterial results of blank, ZT11, and ZTX110 groups; (b) Antibacterial rates of ZT11 and ZTX110 alloys against *E. coli*

4 Discussion

Because the bulk Mg alloys and porous Mg alloy scaffolds were prepared using the same batch of infiltration casting, they can be regarded as having the same type and distribution as the second phase. The grain size, type, and distribution of the second phase directly influence the mechanical properties and corrosion resistance of alloys [32].

4.1 Influence of Ca element on mechanical properties

The addition of Ca improves the mechanical properties of Mg alloys. Ca itself can refine the microstructure of Mg alloy. According to the Hall−Petch formula, the mechanical properties of the alloy are improved with a decrease in the grain size [33]. The studies have shown that the grain refinement of Mg alloys has a more significant strengthening effect than that of other alloy systems (such as Al alloys) [34,35]. This is because the Mg alloy has fewer slip systems than other cubic structure alloys, so the *k* value is often larger (280−320 MPa·$\mu m^{-1/2}$). In contrast, the addition of Ca causes a new second phase, CaMgSn, to appear in the ZTX110 alloy. Because the CaMgSn phase is uniform and fine, it can play a role in strengthening the precipitated phase. Therefore, the same phenomenon is observed in porous materials, and the ZTX110 alloy with the same structure has better mechanical properties and compressive modulus than the ZT11 alloy. Scaffolds with different pore sizes (LP, MP, and SP) have different mechanical properties, indicating that the mechanical properties of the scaffolds can be significantly adjusted by adjusting the pore sizes of the porous scaffolds [24].

4.2 Influence of Ca element on corrosion resistance

The electrochemical potential difference between the Mg matrix and the second phase is a key factor that affects the corrosion mode of Mg alloys [36−38]. Figure 15 shows KPFM images of the tested ZT11 and ZTX110 alloys and the corresponding Volta potential distributions along the white lines in the images. The potential of Mg_2Sn phase in the ZT11 alloy is approximately 298 mV higher compared to that of the Mg matrix, which indicates that Mg_2Sn is the cathodic phase in the corrosive medium and the Mg matrix is the anodic phase; thus, the Mg matrix is preferentially corroded. After the addition of Ca, the potential of newly generated CaMgSn phase in the ZTX110 alloy is approximately 229 mV lower compared with that of Mg matrix, indicating that in the corrosive medium, the CaMgSn phase is the anodic phase and the Mg matrix is the cathodic phase; thus, the CaMgSn phase is preferentially corroded.

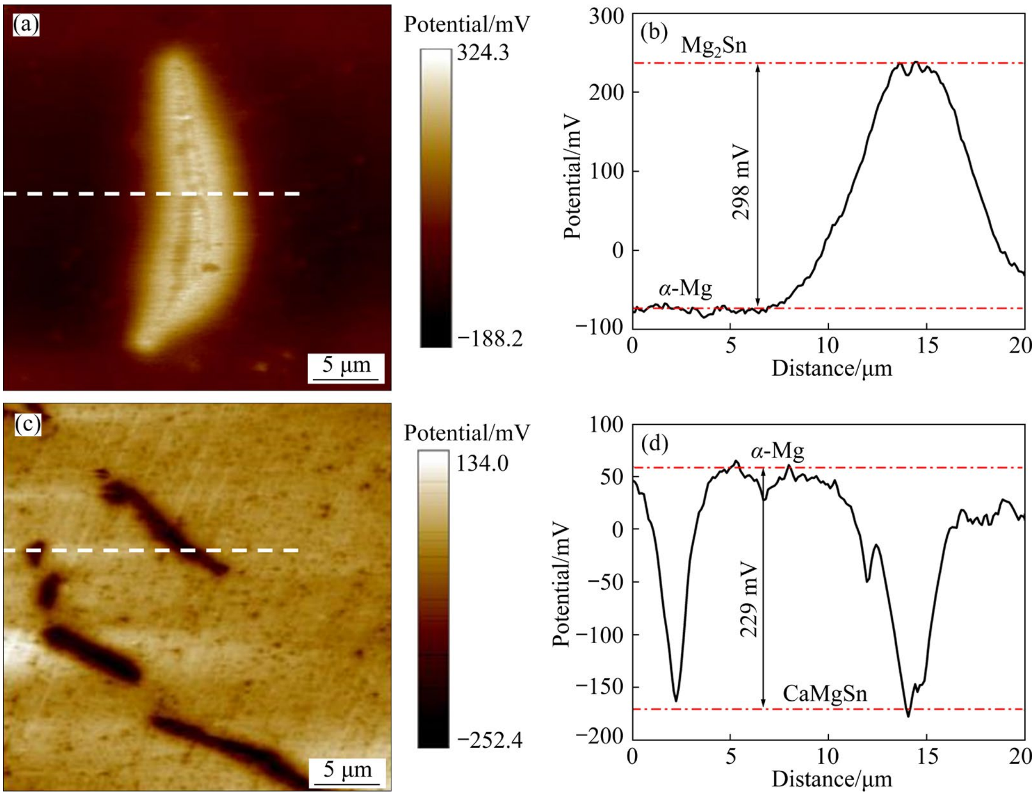

Fig. 15 KPFM images of ZT11 and ZTX110 alloys (a, c) and their corresponding Volta potential distributions along white lines in images (b, d): (a, b) ZT11 alloy; (c, d) ZTX110 alloy

The ZT11 and ZTX110 alloys have different forms of corrosion in the corrosion medium. Figure 16 shows the in-situ corrosion morphologies of the bulk ZT11 and ZTX110 alloys immersed in Hank's solution at different time points. As can be seen from Figs. 7(c, g), the second phase in Fig. 16(a_1) is Mg_2Sn parceling Mg_7Zn_3; therefore, the galvanic corrosion of the ZT11 alloy mainly stems from the Mg_2Sn phase and the Mg matrix. The Mg matrix, as the anode phase, is preferentially

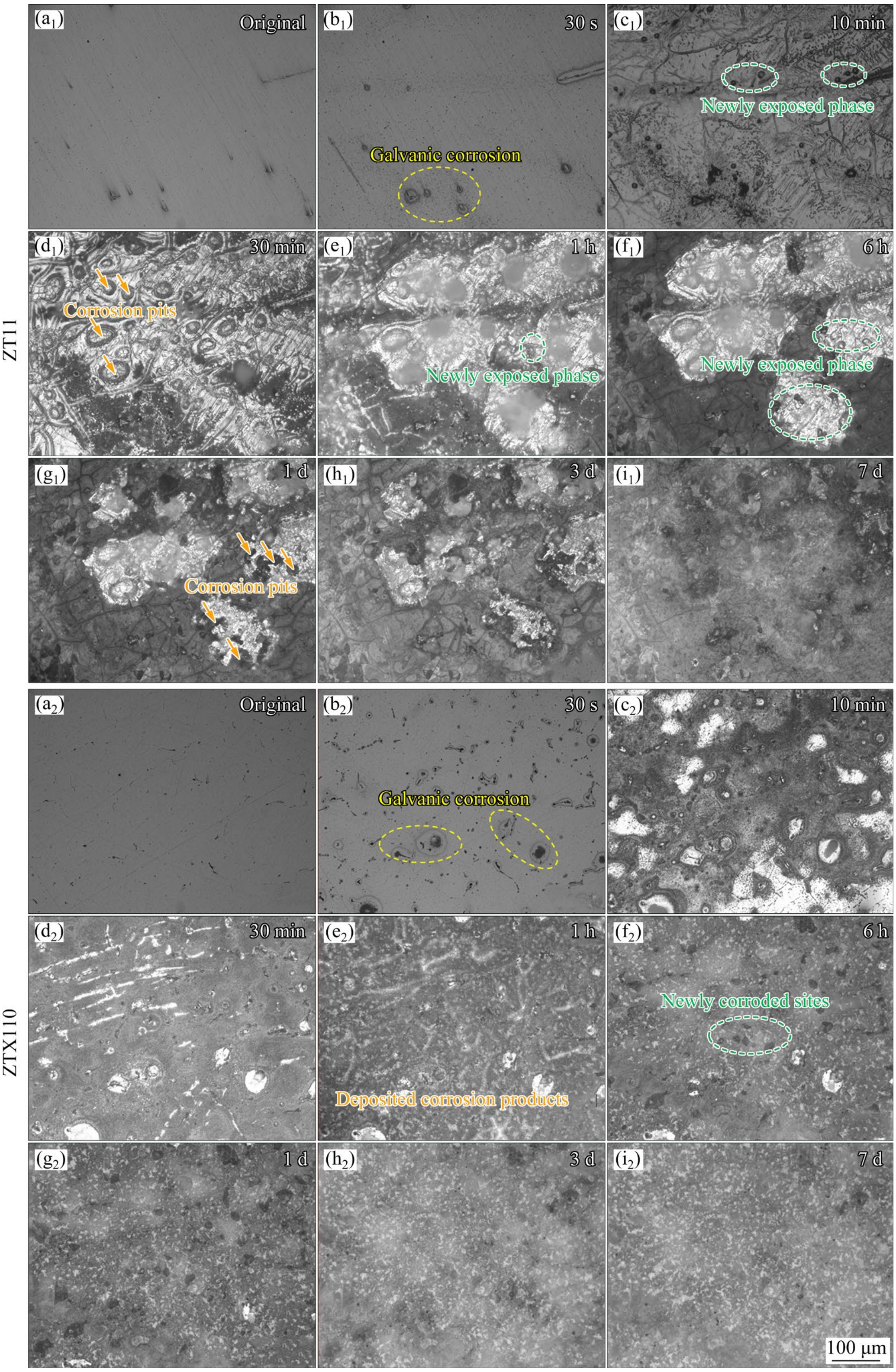

Fig. 16 In-situ corrosion morphologies of bulk ZT11 (a_1−i_1) and ZTX110 (a_2−i_2) alloys immersed in Hank's solution for different time points

corroded, and the Mg matrix is corroded rapidly owing to the significant potential difference (298 mV) between Mg_2Sn and the Mg matrix. As shown in Fig. 16(b_1), galvanic corrosion preferentially occurs in the Mg matrix around the second phase of the ZT11 alloy when immersed for 30 s. As time goes by, at 10 min, the corroded Mg matrix causes the new second phase to be exposed to the solution; thus, the newly exposed second phase forms new galvanic corrosion pairs with the surrounding Mg matrix, which promotes further corrosion of the Mg matrix near the newly exposed second phase (Fig. 16(c_1)). After 30 min, the initial second phase falls off because of the degradation of the surrounding Mg matrix, forming many galvanic corrosion pits (Fig. 16(d_1)). After 1 h, the new second phase is still exposed from the matrix (Fig. 16(e_1)). In comparison, the corrosion of the Mg matrix extends from the surface to the depth. Simultaneously, the surface area of the Mg matrix in the visual field gradually decreases and is almost completely degraded by Day 7. The exposed area of the lower layer increases, and corrosion continues.

In contrast, the galvanic corrosion of the ZTX110 alloy mainly originates from the CaMgSn phase and Mg matrix. The CaMgSn phase is preferentially corroded as the anode phase, and the Mg matrix is protected as the cathode. When the ZTX110 alloy is immersed in Hank's solution for 30 s, the uniform and fine second phases (as shown in Figs. 7(d, h)) begin to corrode. Owing to the large potential difference (229 mV) between the second phase and the matrix, corrosion is rapid, and uniform and fine second phase corrosion pits (Fig. 16(b_2)) appear on the sample surface. During the second phase of corrosion, the Mg matrix is in a protected state, and almost no corrosion occurs. After 10 min, because most of the second phase on the surface has degraded, the Mg matrix itself begins to corrode, and the corrosion rate of the Mg matrix is slow because there is almost no potential difference distribution on the surface (Figs. 16(c_2−e_2)). After 6 h, the new second phase is exposed to the solution and rapidly corroded, resulting in the formation of the second phase corrosion pit. Once again, the Mg matrix is protected and slowly degraded. In addition, the degradation of the Mg matrix leads to the appearance of uniform and fine corrosion products on the surface of the sample (Figs. 16(e_2−i_2)), which hinders the corrosion of Mg matrix.

Figure 17 shows the corrosion mechanism of the porous Mg alloy scaffolds. Theoretically, for the same alloys, the depth of surface corrosion in the

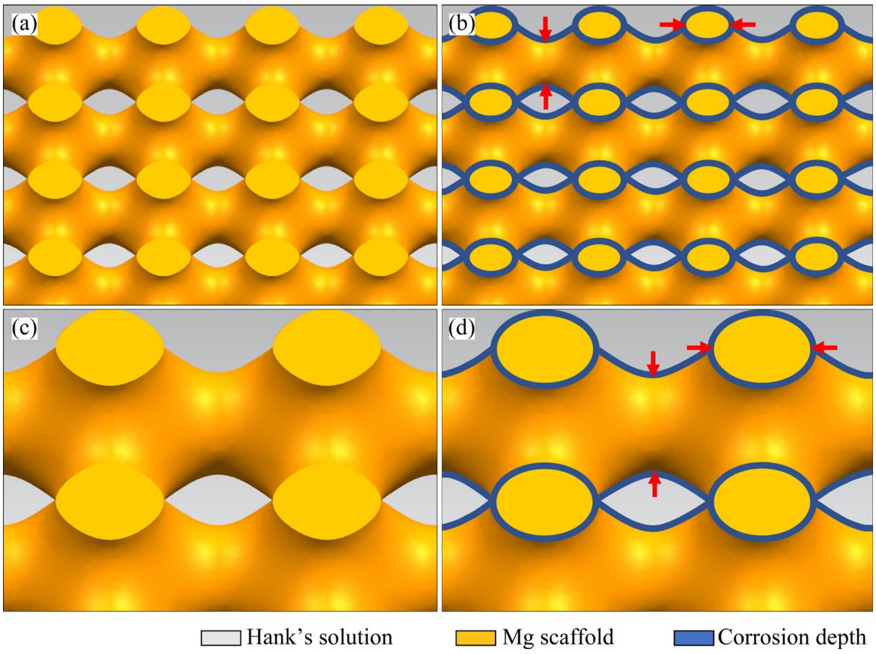

Fig. 17 Corrosion mechanism diagram of porous Mg alloy scaffolds: (a) Diagram of Mg (SP) alloy scaffold before corrosion; (b) Diagram of Mg (SP) alloy scaffold after corrosion for period of time; (c) Diagram of Mg (LP) alloy scaffold before corrosion; (d) Diagram of Mg (LP) alloy scaffold after corrosion for period of time

interior of the Mg alloy scaffold is the same; however, different pore sizes of the scaffolds show different corrosion resistances. As shown in Fig. 17, with an increase in the pore sizes, the edges of the scaffolds (as shown by the red arrows) also increase, and the specific surface areas of the scaffolds decrease. When the scaffolds are immersed in Hank's solution, the scaffold is gradually corroded from the surface to the inside with an increase of immersion time. The inward corrosion depth of the scaffolds with larger specific surface areas is almost the same as that of the scaffolds with smaller specific surface areas. Therefore, the edges of scaffolds with small pores are preferentially corroded and failed first, resulting in a higher corrosion rate. The corrosion resistance decreases in the order: LP > MP > SP.

5 Conclusions

(1) The pure Ti pore structure template prepared by 3D printing is well formed, and the intermediate complex of pure Ti and Mg alloy prepared by infiltration casting exhibits excellent interface bonding without casting defects. The Mg alloy scaffold eluted with the HF solution exhibits a complete pass structure. During 3D printing process, the heat transfer effect causes the actual porosities and pore sizes to exceed the designed ones.

(2) The addition of Ca changes the second phase of ZTX110 alloy from Mg_2Sn to CaMgSn and refines its microstructure. The LP-ZTX110 alloy scaffold exhibits the best mechanical properties, with a compressive yield strength of 32.61 MPa and a compressive modulus of 0.23 GPa.

(3) The addition of Ca changes the microstructure of the ZTX110 alloy and improves its corrosion resistance. The corrosion current density decreases from 58.74 to 14.64 $\mu A/cm^2$, and the corrosion rate of the LP-ZTX110 alloy scaffold at 199 h hydrogen evolution is 0.88 mm/a.

(4) The ZT11 and ZTX110 alloys exhibit excellent biocompatibility and no cytotoxicity. Compared with the ZT11 alloy scaffold, the MC-3T3 cells have a larger adhesion area on the surface of the ZTX110 alloy scaffold. In addition, the ZT11 and ZTX110 alloys exhibit a good antibacterial effect on *E. coli*, with an antibacterial rate higher than 97.81%.

CRediT authorship contribution statement

Lei-ting YU: Conceptualization, Methodology, Investigation, Formal analysis, Data curation, Visualization, Writing − Original draft; **Hao LIU:** Investigation, Methodology, Formal analysis; **Peng-nan JIANG:** Investigation, Methodology; **Shao-yuan LYU:** Investigation, Formal analysis, Funding acquisition; **Yun ZHAO:** Investigation, Formal analysis, Funding acquisition; **Wei LI:** Conceptualization, Supervision, Writing − Review & editing, Funding acquisition; **Min-fang CHEN:** Conceptualization, Supervision, Writing − Review & editing, Funding acquisition.

Declaration of competing interest

The authors declare that they have no known competing financial interests or personal relationships that could have appeared to influence the work reported in this paper.

Data availability

The raw/processed data required to reproduce these findings cannot be shared at this time due to technical or time limitations.

Acknowledgments

The authors acknowledge the financial support for this work from the National Natural Science Foundation of China (Nos. 52171241, 52373251, 52201301, 51801137), Natural Science Foundation of Tianjin City, China (No. 22JCQNJC00750), and Tianjin University of Technology Graduate Research Innovation Project, China (No. YJ2235).

References

[1] YAN Ting-liang, WANG Xiang, FAN Jin-long, NIE Qi-dong. Microstructure and properties of biodegradable co-continuous (HA+β-TCP)/Zn−3Sn composite fabricated by vacuum casting-infiltration technique [J]. Transactions of Nonferrous Metals Society of China, 2021, 31: 3075−3086.

[2] ZHANG Jian, LI Hai-yan, WANG Wu, HUANG Hua, PEI Jia, QU Hai-yun, YUAN Guang-yin, LI Dong-dong. The degradation and transport mechanism of a Mg−Nd−Zn−Zr stent in rabbit common carotid artery: A 20-month study [J]. Acta Biomaterialia, 2018, 69: 372−384.

[3] XIAO Chi, WANG Li-qing, REN Yu-ping, SUN Shi-neng, ZHANG Er-lin, YAN Chong-nan, LIU Qi, SUN Xiao-gang, SHOU Fen-yong, DUAN Jing-zhu, WANG Hua, QIN Gao-wu. Indirectly extruded biodegradable Zn−0.05wt.%Mg alloy with improved strength and ductility: In vitro and in vivo studies [J]. Journal of Materials Science & Technology, 2018, 34: 1618−1627.

[4] HAN Shu-yang, YAO Run-hua, HANG Rui-qiang, YAO Xiao-hong. Preparation and properties of biodegradable

Zn−Nb composite materials [J]. Journal of Taiyuan University of Technology, 2022, 53: 588−599. (in Chinese)

[5] MOSTAED E, SIKORA-JASINSKA M, DRELICH J W, VEDANI M. Zinc-based alloys for degradable vascular stent applications [J]. Acta Biomaterialia, 2018, 71: 1−23.

[6] JIN Hua-lan, ZHAO Shan, GUILLORY R, BOWEN P K, YIN Zhi-yong, GRIEBEL A, SCHAFFER J, EARLEY E J, GOLDMAN J, DRELICH J W. Novel high-strength, low-alloys Zn−Mg (<0.1 wt.% Mg) and their arterial biodegradation [J]. Materials Science and Engineering C, 2018, 84: 67−79.

[7] QIAN Yi, YUAN Guang-yin. Research status, challenges, and countermeasures of biodegradable Zinc-based vascular stents [J]. Acta Metallurgica Sinica, 2021, 57: 272−282. (in Chinese)

[8] MUTLU I. Production and fluoride treatment of Mg−Ca−Zn−Co alloy foam for tissue engineering applications [J]. Transactions of Nonferrous Metals Society of China, 2018, 28: 114−124.

[9] QIN Yu, WEN Peng, GUO Hui, XIA Dan-dan, ZHENG Yu-feng, JAUER L, POPRAWE R, VOSHAGE M, SCHLEIFENBAUM J H. Additive manufacturing of biodegradable metals: Current research status and future perspectives [J]. Acta Biomaterialia, 2019, 98: 3−22.

[10] LI Yan-hong, ZHOU Jie, PAVANRAM P, LEEFLANG M A, FOCKAERT L I, POURAN B, TUMER N, SCHRODER K U, MOL J M C, WEINANS H, JAHR H, ZADPOOR A A. Additively manufactured biodegradable porous magnesium [J]. Acta Biomaterialia, 2018, 67: 378−392.

[11] GU Xue-nan, XIE Xin-hui, BARR L N, ZHENG Yu-feng, QIN Lin. In vitro and in vivo studies on a Mg−Sr binary alloy system developed as a new kind of biodegradable metal [J]. Acta Biomaterialia, 2012, 8: 2360−2374.

[12] CAI Shu-hua, LEI Ting, LI Nian-feng, FENG Fang-fang. Effects of Zn on microstructure, mechanical properties and corrosion behavior of Mg−Zn alloys [J]. Materials Science and Engineering C, 2012, 32: 2570−2577.

[13] ZHAO Li-chen, ZHANG Zhe, SONG Yu-ting, LIU Shuang-jin, QI Yu-min, WANG Xin, WANG Qing-zhou, CUI Chun-xiang. Mechanical properties and in vitro biodegradation of newly developed porous Zn scaffolds for biomedical applications [J]. Materials & Design, 2016, 108: 136−144.

[14] KUBÁSEK J, VOJTĚCH D, LIPOV J, RUML T. Structure, mechanical properties, corrosion behavior and cytotoxicity of biodegradable Mg−X (X=Sn, Ga, In) alloys [J]. Materials Science and Engineering C, 2013, 33: 2421−2432.

[15] BAKHSHESHI-RAD H R, DAYAGHI E, ISMAIL A F, AZIZ M, AKHAVAN-FARID A, CHEN Xiong-biao. Synthesis and in-vitro characterization of biodegradable porous magnesium-based scaffolds containing silver for bone tissue engineering [J]. Transactions of Nonferrous Metals Society of China, 2019, 29: 984−996.

[16] YANG Ming-bo, CHENG Liang, PAN Fu-sheng. Effects of calcium addition on as-cast microstructure and mechanical properties of Mg−5Zn−5Sn alloy [J]. Transactions of Nonferrous Metals Society of China, 2010, 20: 769−775.

[17] WEI Ju-ying, CHEN Ji-hua, YAN Hong-ge, SU Bin, PAN Xue-qiang. Effects of minor Ca addition on microstructure and mechanical properties of the Mg−4.5Zn−4.5Sn−2Al-based alloy system [J]. Journal of Alloys and Compounds, 2013, 548: 52−59.

[18] BERKMORTEL J J, HU H, KEARNS J E, ALLISON J E. Die castability assessment of magnesium alloys for high temperature applications: Part 1 of 2 [J]. SAE Technical Paper, 2000, 109: 574−581.

[19] KIM B H, PARK K C, PARK Y H, PARK I M. Effect of Ca and Sr additions on high temperature and corrosion properties of Mg−4Al−2Sn based alloys [J]. Materials Science and Engineering A, 2011, 528: 808−814.

[20] ZHENG Yu-feng, GU Xue-nan, WITTE F. Biodegradable metals [ ]. Materials Science and Engineering R: Reports, 2014, 77: 1−34.

[21] LEVY G K, VENTURA Y, GOLDMAN J, VAGO R, AGHION E. Cytotoxic characteristics of biodegradable EW10X04 Mg alloy after Nd coating and subsequent heat treatment [J]. Materials Science and Engineering C, 2016, 62: 752−761.

[22] COCKERILL I, SU Ying-chao, SINHA S, QIN Yi-xian, ZHENG Yu-feng, YOUNG M L, ZHU Dong-hui. Porous zinc scaffolds for bone tissue engineering applications: A novel additive manufacturing and casting approach [J]. Materials Science and Engineering C, 2020, 110: 10738.

[23] YU Lei-ting, ZHAO Zi-han, TANG Chao-kun, LI Wei, YOU Chen, CHEN Min-fang. The mechanical and corrosion resistance of Mg−Zn−Ca−Ag alloys: The influence of Ag content [J]. Journal of Materials Research and Technology, 2020, 9: 10863−10875.

[24] LIU Jin-ge, LIU Bing-chuan, MIN Shu-yuan, YIN Bang-zhao, PENG Bo, YU Zi-shi, WANG Cai-mei, MA Xiao-lin, WEN Peng, TIAN Yun, ZHENG Yu-feng. Biodegradable magnesium alloy WE43 porous scaffolds fabricated by laser powder bed fusion for orthopedic applications: Process optimization, in vitro and in vivo investigation [J]. Bioactive Materials, 2022, 16: 301−319.

[25] MARVI-MASHHADI M, ALI W, LI Mu-zi, GONZALEZ C, LLORCA J. Simulation of corrosion and mechanical degradation of additively manufactured Mg scaffolds in simulated body fluid [J]. Journal of the Mechanical Behavior of Biomedical Materials, 2022, 126: 104881.

[26] DU Wen-bo, LIU Ke, MA Ke, WANG Zhao-hui, LI Shu-bo. Effects of trace Ca/Sn addition on corrosion behaviors of biodegradable Mg−4Zn−0.2Mn alloy [J]. Journal of Magnesium and Alloys, 2018, 6: 1−14.

[27] WANG Xue-jian, ZHANG Yu-bo, GUO En-yu, CHEN Zong-ning, KANG Hui-jun, LIU Xue-qin, HAN Pei, WANG Tong-min. In vitro investigation on microstructure, bio-corrosion properties and cytotoxicity of as-extruded Mg−5Sn−xIn alloys [J]. Journal of Alloys and Compounds, 2021, 877: 160294.

[28] WU Luo-yi, LI Yu-an, CHEN Ying-liang, LINGHU Feng, JIANG Fu-lin, CHEN Gang, TENG Jie, FU Ding-fa, ZHANG Hui. Microstructure evolution and corrosion resistance improvement of Mg−Gd−Y−Zn−Zr alloys via surface hydrogen treatment [J]. Corrosion Science, 2021, 191: 109746.

[29] SABBAGHIAN M, MAHMUDI R, SHIN K S. Effect of texture and twinning on mechanical properties and corrosion behavior of an extruded biodegradable Mg−4Zn alloy [J].

Journal of Magnesium and Alloys, 2019, 7: 707−716.

[30] IQBAL J, JAN T, ISMAIL M, AHMAD N, ARIF A, KHAN M, ADIL M, SAMI U A, ARSHAD A. Influence of Mg doping level on morphology, optical, electrical properties and antibacterial activity of ZnO nanostructures [J]. Ceramics International, 2014, 40: 7487−7493.

[31] JIANG Wei-yan, WANG Jing-feng, LIU Qing-shan, ZHAO Wei-kang, JIANG Dian-ming, GUO Shen-feng. Low hydrogen release behavior and antibacterial property of Mg−4Zn−*x*Sn alloys [J]. Materials Letters, 2019, 241: 88−91.

[32] MA Ying-zhong, WANG De-xin, LI Hong-xiang, YANG Chang-lin, YUAN Fu-song, ZHANG Ji-shan. Microstructure, mechanical properties and corrosion behavior of quaternary Mg−1Zn−0.2Ca−*x*Ag alloy wires applied as degradable anastomotic nails [J]. Transactions of Nonferrous Metals Society of China, 2021, 31: 111−124.

[33] WANG Bo-ning, WANG Feng, WANG Zhi, LIU Zheng, MAO Ping-li. Fabrication of fine-grained, high strength and toughness Mg alloy by extrusion−shearing process [J]. Transactions of Nonferrous Metals Society of China, 2021, 31: 666−678.

[34] RAZAVI S M, FOLEY D C, KARAMAN I, HARTWIG K T, DUYGULU O, KECSKES L J, MATHAUDHU S N, HAMMOND V H. Effect of grain size on prismatic slip in Mg−3Al−1Zn alloy [J]. Scripta Materialia, 2012, 67: 439−442.

[35] PAN Hu-cheng, QIN Gao-wu, HUANG Yun-miao, REN Yu-ping, SHA Xue-chao, HAN Xiao-dong, LIU Zhi-quan, LI Cai-fu, WU Xiao-lei, CHEN Hou-wen, HE Cong, CHAI Lin-jiang, WANG Yun-zhi, NIE Jian-feng. Development of low-alloyed and rare-earth-free magnesium alloys having ultra-high strength [J]. Acta Materialia, 2018, 149: 350−363.

[36] COY A E, VIEJO F, SKELDON P, THOMPSON G E. Susceptibility of rare-earth-magnesium alloys to micro-galvanic corrosion [J]. Corrosion Science, 2010, 52: 3896−3906.

[37] ATRENS A, SONG Guang-lin, LIU Ming, SHI Zhi-ming, CAO Fu-yong, DARGUSCH M S. Review of recent developments in the field of magnesium corrosion [J]. Advanced Engineering Materials, 2015, 17: 400−453.

[38] ESMAILY M, SAVENSSON J E, FAJARDO S, BIRBILIS N, FRANKEL G S, VIRTANEN S, ARRABAL S, JOHANSSON L G. Fundamentals and advances in magnesium alloy corrosion [J]. Progress in Materials Science, 2017, 89: 92−193.

Ca 元素添加对 3D 打印 Ti 模板渗流铸造 Mg−1Zn−1Sn 合金支架显微组织与性能的影响

宇雷霆[1]，刘　昊[1]，姜芃男[1]，吕绍元[1,2]，赵　云[1,2]，李　伟[1,2,3]，陈民芳[1,2,3]

1. 天津理工大学 材料科学与工程学院，天津 300384；
2. 天津理工大学 功能材料国家级实验教学示范中心，天津 300384；
3. 天津理工大学 光电材料与器件教育部重点实验室，天津 300384

摘　要：采用 3D 打印 Ti 支架为模板，渗流浇铸制备了 Mg−1Zn−1Sn 和 Mg−1Zn−1Sn−0.2Ca 合金支架，以实现支架内部完全连通和孔隙结构精准控制。结果表明：各种孔径的 P 模型的实际孔隙率和孔径均大于设计值。Ca 元素的加入使合金的第二相由 Mg_2Sn 相转变为 CaMgSn 相，并且能细化显微组织。Mg−1Zn−1Sn−0.2Ca 合金支架的抗压屈服强度和压缩模量分别达到 32.61 MPa 和 0.23 GPa，其电化学腐蚀电流密度可达 14.64 μA/cm^2，瞬时腐蚀速率为 0.335 mm/a。两种合金支架均无细胞毒性，不仅表现出优异的生物相容性，而且对大肠杆菌的抗菌效果均高于 97.81%。Mg 合金支架具有巨大的临床应用潜力。

关键词：渗流铸造；3D 打印 Ti 模板；力学性能；耐蚀性能；生物相容性

(Edited by Bing YANG)